ChemElectroChem

Research Article
doi.org/10.1002/celc.202200018

Chemistry Europe
European Chemical Societies Publishing

www.chemelectrochem.org

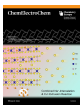

A Combined Sodium Intercalation and Copper Extrusion Mechanism in the Thiophosphate Family: $CuCrP_2S_6$ as Anode Material in Sodium-Ion Batteries

Jonas van Dinter, David Grantz, Alexander Bitter, and Wolfgang Bensch*[a]

The layered hypothiophosphate $CuCrP_2S_6$ was identified as promising candidate for the application as anode in sodium-ion batteries exhibiting an appropriate electrochemical performance (409 $mAh\,g^{-1}$ after 200 cycles @ 1 $A\,g^{-1}$). The electrochemical long-term experiments suggest that the reaction mechanism changed upon repeated discharging and charging. The initial discharge and charge process was studied by X-ray diffraction evidencing that at the early discharge stages, Na^+ was intercalated into the interlayer space accompanied by a simultaneous reduction of Cu^+ to metallic Cu, which was extruded from the host. At later stages of discharge, a conversion of the intermediate phase to Cu^0, amorphous Cr^0 and P^0 embedded in nanocrystalline Na_2S occurred. After recharging, only reflections of nanocrystalline NaF could be identified, which is part of the generated solid electrolyte interphase (SEI) layer. In contrast to observation made in literature, elemental Cu seems to be oxidized during the charge process again.

Introduction

Although Lithium-ion batteries (LIBs) dominate the market for portable devices and electromobility, this energy storage system is not considered suitable to satisfy climate change related challenges and requirements according to the prevailing opinion in literature. With increasing energy conversion from renewable sources, the necessity for stationary energy storage systems (ESS) will also increase to balance out over- and underproduction of electric energy produced by renewable sources. In this context, the application of Na based storage systems seems to be more reasonable than Li based systems.[1–6] The biggest drawbacks of Na opposed to Li are the higher mass, larger ionic radius and the smaller electrochemical potential of Na, causing lower energy densities for the corresponding Na based battery systems.[4,7,8] However, most of these apparent negative traits are negligible applying sodium-ion batteries (SIBs) for stationary ESS, since *e.g.* weight is less important for stationary applications. Additionally, the low cost of Na due to its high abundance and wide distribution is an important commercial advantage over Li.[1–4] Nevertheless, while graphite is the anode material of choice in LIBs, it only shows a low specific capacity using Na as guest species.[9] It is assumed that the intercalation of Na^+ cations into graphite is thermodynamically hindered and hence graphite is not suitable for the usage in SIBs as anode material.[9–13] Therefore, identification and development of anode materials for SIBs providing high specific capacities and good long-term performance is necessary. While hard carbon has been identified as promising anode material, which is capable of reversible sodium intercalation, many non-trivial improvements are necessary in order to obtain an ideal electrode. Those improvements include tuning of surface area, interlayer space, amount of defects, size of pores and the choice of the precursor, while the exact impact of the individual treatments is not understood completely.[14–16] In contrast, the use of active materials that undergo conversion reactions leads to higher specific capacities, allowing more electrons to participate in the electrochemical reaction opposed to intercalation reactions.[17] Until now, a large variety of materials have been investigated ranging from carbonaceous materials[4,13–16] to binary and ternary metal chalcogenides,[18–23] alloys,[20,24,25] elemental phosphorous[26,27] and many other compounds.[4,28] Especially the smaller ionicity of sulfides is considered beneficial for conversion reactions and reversible Na storage. Compared to *e.g.* a M–O bond, the M–S bond is less polar, which reduces overpotentials during the charge and discharge processes.[29] However, another interesting substance class exhibiting M–S bonds is represented by layered transition metal (hypo)thiophosphates (MTPs), which are less often studied as active materials in SIBs. Originally already discovered in the 19th century,[30] MTPs initially gained broader research interest during the 1970s[31] because they share many properties with layered transition metal dichalcogenides (TMDCs) and exhibit intermediate to wide bandgaps in the range between 1.3 and 3.5 eV.[31–34] However, MTPs also have been identified as promising anode materials in LIBs and SIBs recently.[32,35,36] Usually, MTPs are categorized as M^{II} ($M_2P_2S_6$) or $M^{I}M^{III}$ ($M'M''P_2S_6$) based compounds. While MTPs with bivalent metallic cations typically crystallize in *C2/m* symmetry, when mixed cations

[a] *J. van Dinter, D. Grantz, A. Bitter, Prof. Dr. W. Bensch*
Institute of Inorganic Chemistry
Kiel University
Max-Eyth-Str. 2, 24118 Kiel, Germany
E-mail: wbensch@ac.uni-kiel.de

Supporting information for this article is available on the WWW under https://doi.org/10.1002/celc.202200018

($M^{I}M^{III}$) occupy the metal sites also trigonal symmetry is common.[31,33,37–40] The structure of monoclinic hypothiophosphates is mostly formed by close-packed S^{2-} anion layers, where the resulting octahedral sites are occupied by metal cations and by P–P dimers. Each P atom is coordinated by three S and one P atom forming an ethane-like $[P_2S_6]^{4-}$ dumbbell. These units occupy 1/3 of the octahedral sites, whereas the remaining sites are occupied by metal cations. This results in a honeycomb arrangement, where three $[P_2S_6]^{4-}$ units surround one MS_6 octahedron.[31,33,41,42] Interestingly, $M^{I}M^{III}$ based MTPs with M^{I}=Cu^{+} often exhibit special behavior, because the Cu^{+} cation is not bound to the center, but can occupy different sites in the sulfur defined octahedron dependent on temperature. At room temperature, the Cu^{+} cations are unevenly distributed between two different octahedral sites (Figure 1a), whereas at low temperatures, Cu^{+} strictly alternates between upper and lower octahedral sites (Figure 1b).[31,33,43,44]

Concerning possible battery applications, especially ternary Cu containing sulfides might exhibit beneficial properties. The electrochemical reaction during discharging leads to reduction of Cu^{+} to metallic Cu, which is extruded as nanoparticles or dendrites.[46–48] As a result, the electric conductivity considerably increases in the electrodes. The presence of elemental Cu enhances the rate capability, capacity retention and long-term stability.[49,50] For example, CuV_2S_4 exhibits a high reversible specific capacity of 580 mAh g^{-1} after 300 cycles at a current rate of 0.7 A g^{-1}.[49] $CuCrS_2$ on the other hand delivered a reversible specific capacity of 252 mAh g^{-1} after 500 cycles at a current density of 1.5 A g^{-1}, which is still 81% of the capacity obtained after the 2nd and 99% of the capacity obtained after the 50th cycle, demonstrating extraordinary electrochemical properties.[50] For these systems, the presence of Cu^{+} is considered beneficial by being reduced to elemental Cu during discharge, thus preventing formation of polysulfides and/or enhancing electric conductivity, consequently improving cycling stability and rate capability.[49,50] To incorporate these beneficial properties into MTPs, the most obvious choice as anode material is $CuCrP_2S_6$. To the best of our knowledge, $CuCrP_2S_6$ never has been investigated before as anode material in SIBs. In a recent study, we used $Ni_2P_2S_6$ for the application as anode material in SIBs and thoroughly characterized the underlying reaction mechanisms.[36] Assuming a similar reaction pathway for $CuCrP_2S_6$, the theoretical capacity amounts to 870 mAh g^{-1} [Eq. (1)]:

$$CuCrP_2S_6 + 12\ Na^{+} + 12\ e^{-} \rightarrow Cu + Cr + 2\ P + 6Na_2S \quad (1)$$

Based on the idea of beneficial effects of copper containing active materials and the promising results of previously studied MTPs, we present the electrochemical properties of $CuCrP_2S_6$ as potential anode material in SIBs. Additionally, investigations of the reaction products after the discharge and charge process were conducted.

Results and Discussion

Characterization of pristine $CuCrP_2S_6$

The compound $CuCrP_2S_6$ could be obtained phase pure through manual separation from $CrPS_4$ as by-product. Despite extensive variation of the synthesis parameters, formation of small amounts of $CrPS_4$ could not be avoided completely (see ESI; Figure S1). $CuCrP_2S_6$ crystallizes in the monoclinic space group *C2/c* at room temperature with lattice parameters of a = 5.916 Å, b = 10.246 Å, c = 13.415 Å and β = 107.09°, V = 777.250 $Å^3$.[43] The PXRD pattern of the sample compared to the calculated PXRD pattern of the room temperature modification of $CuCrP_2S_6$ demonstrates phase purity (Figure 2). However, the intensity ratios of some reflections differ from the calculated pattern and the extinction of less intense reflections can be observed. Structural phenomena such as stacking faults, twinning or rotational disorder most likely cause these deviations in intensity for this kind of layered material. Especially for

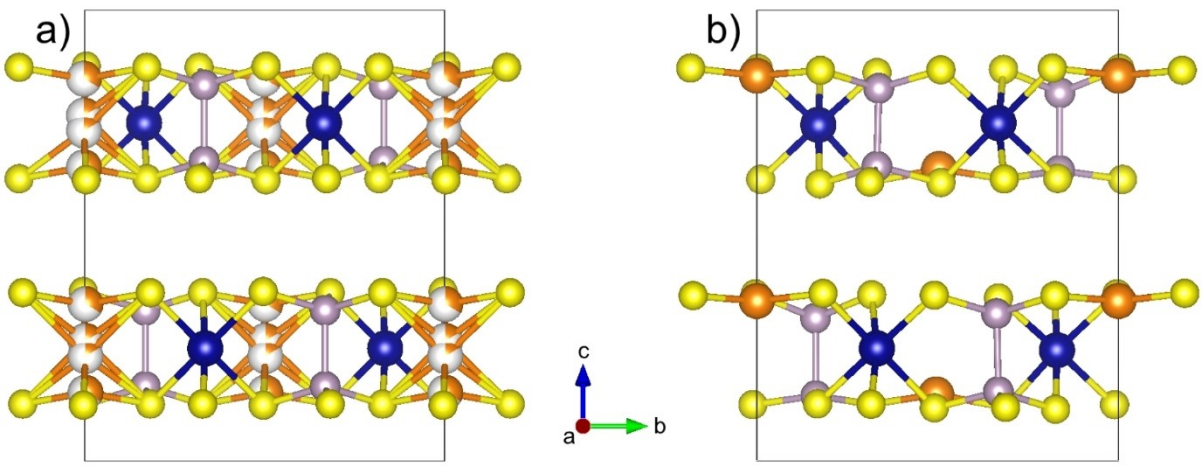

Figure 1. View of the two structural modifications of $CuCrP_2S_6$ (orange: Cu^{+}; blue: Cr^{3+}; purple: P^{4+}; yellow: S^{2-}) at room temperature (a), space group *C2/c*, and low temperatures (b), space group *Pc*. The viewing direction is along the *a*-axis. Structures were created with the software VESTA 3.4.0[45] using crystallographic data from the literature.[43,44]

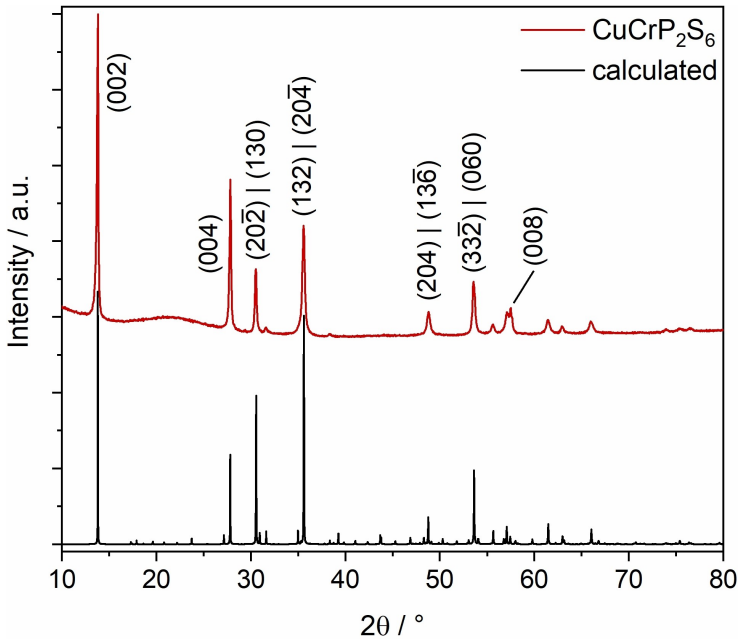

Figure 2. PXRD pattern of $CuCrP_2S_6$ compared to the calculated pattern using literature data.[43]

hypothiophosphates $[P_2S_6]^{4-}$ these phenomena are often observed and were described in literature.[51–54] In a previous study on $Ni_2P_2S_6$, TEM analysis revealed the existence of structurally distorted domains with monoclinic to pseudo-hexagonal symmetry resulting in similar deviations from the expected PXRD pattern.[36] Regarding the structural similarities, such partial distortions of the unit cell in certain domains might occur as well for $CuCrP_2S_6$ and hence intensity ratios are different than expected. Further, a preferred orientation caused by sample preparation may also influence the observed intensity ratios, since the intensities of the (00 *l*) reflections are significantly stronger than expected.

Additionally, combined EDX data at different spots of the sample and chemical elemental analysis (see ESI; Tables S1, S2) reveal the composition of $Cu_{1.05}Cr_{0.92}P_{1.96}S_{6.07}$, which fits nicely the assumed chemical formula. SEM images (see Figure S2) additionally depict that multiple slabs are stacked on top of each other illustrating the plate-like and layered structure of the compound.

Electrochemical performance

Results of long-term stability and rate capability measurements of $CuCrP_2S_6$ electrodes are displayed in Figure 3a. Galvanostatic long-term measurements within a potential range between 3.0 and 0.1 V with an applied current density of 1 $A g^{-1}$ showed Coulombic efficiencies close to 100% after the 3rd cycle. The initial discharge capacity is 982 $mAh g^{-1}$ (≈13.6 Na/f.u.), while the specific charge capacity of the initial cycle amounts to 810 $mAh g^{-1}$ (≈11.2 Na/f.u.). During the first 20 cycles, the capacities quickly drop to 514 $mAh g^{-1}$ (≈7.1 Na/f.u.) and remain stable for the following 20 cycles. Thereafter, a local minimum of 461 $mAh g^{-1}$ (≈6.4 Na/f.u.) in the 65th cycle is obtained and 504 $mAh g^{-1}$ (≈7.0 Na/f.u.) is reached after 124 cycles. Afterwards, a steady decrease occurs until a reversible capacity of 409 $mAh g^{-1}$ (≈5.6 Na/f.u.) is obtained in the 200th cycle. Accordingly, a distinct evolution of the discharge and charge profiles (Figure 3b, c) is observed during the long-term measurement. For the first cycle, the discharge profile quickly drops from 2.8 V to a pseudo-plateau around 1.86 V and further decreases to a potential of ~0.6 V, beneath which the potential decline slows down and is relatively shallow until the initial discharge capacity of 982 $mAh g^{-1}$ is obtained. In the charge profile of the 1st cycle, the potential rapidly increases until a pseudo-plateau at around 2.0 V is reached and afterwards continues to rise until the cell is completely charged delivering an initial charge capacity of 810 $mAh g^{-1}$, which corresponds to a capacity loss of ~172 $mAh g^{-1}$ (≈2.4 Na/f.u.). This value seems to be large, but is within the typical order of magnitude for irreversible capacity of these kind of materials[36,55,56] and is mainly caused by formation of a solid electrolyte interphase (SEI) as well as co-intercalation of the solvent molecules of the electrolyte in case of layered active materials. The discharge/charge profiles for the subsequent cycles differ vastly from the profiles of the initial cycle, which is a common observation for conversion-type electrodes. For the 3rd cycle, the potential drops quickly from 3.0 V to ~0.5 V and thereafter continues to decrease much slower until the discharged state is reached. The charge profile of the 3rd cycle (pseudo-plateau at ~2.08 V) looks very similar to the first cycle, but yields less capacity. From the 3rd cycle onwards, the discharge/charge curves display several alterations. Until the 65th cycle, a new pseudo-plateau at ~1.43 V in the discharge profile as well as a small pseudo-plateau at ~1.57 V and a more pronounced plateau at ~1.99 V in the charge curve are

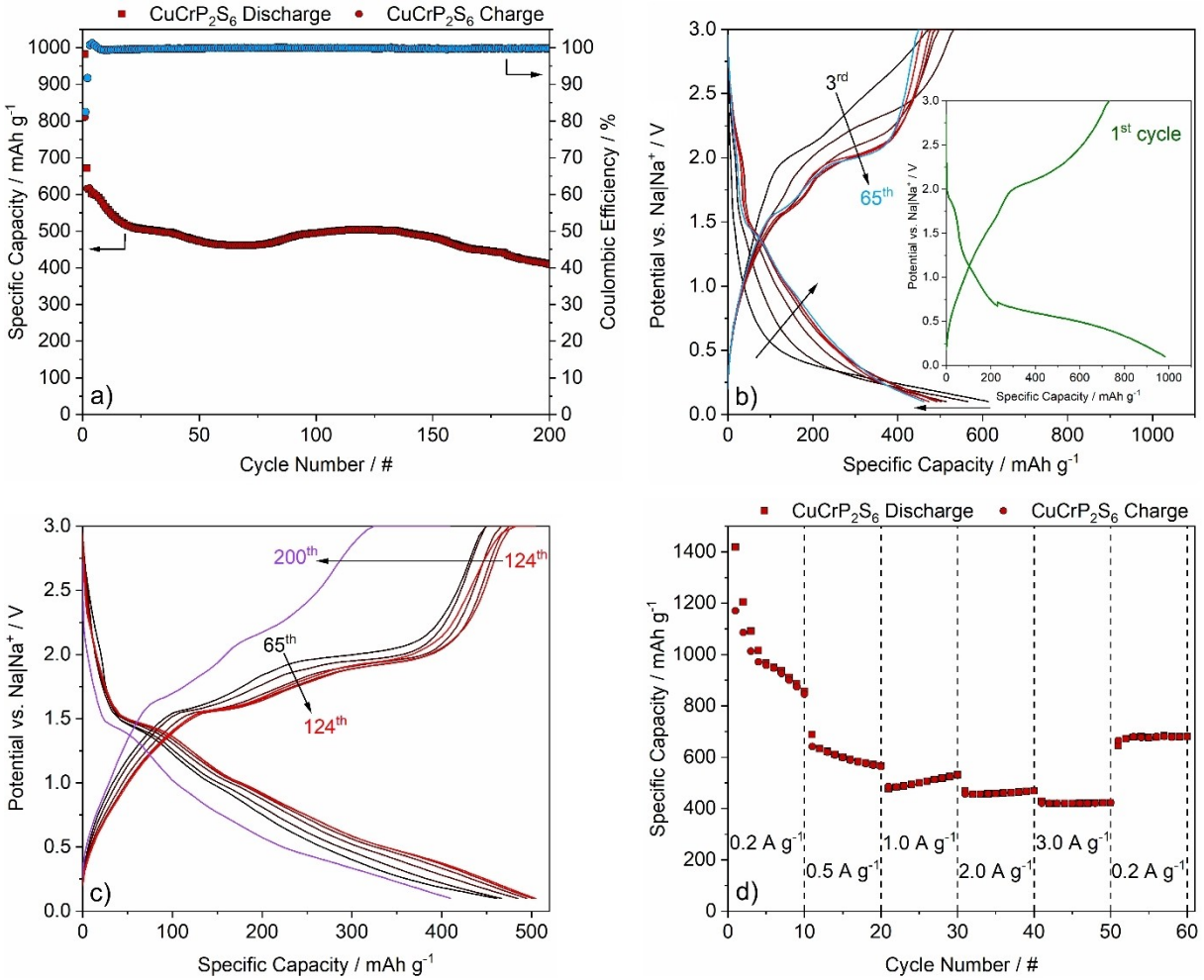

Figure 3. a) Electrochemical long-term performance and Coulombic Efficiency of $CuCrP_2S_6$ electrode against Na metal. A current rate of 1 A g^{-1} was applied and cycling was performed in a potential range between 3.0 and 0.1 V. Discharge and charge curves of 1st–65th (b, inset: 1st cycle) and 65th–124th and the 200th cycle (c). Roughly, every 10th cycle is shown between the cycles 3, 65 and 124. d) Rate capability measurements for several current rates ranging between 0.2 and 3.0 A g^{-1} applied in a potential range between 3.0–0.1 V.

developed. The evolution from the 65th to 124th cycle is less pronounced. However, the pseudo-plateau in the discharge curve slightly shifts to 1.47 V, while being more pronounced. In the charge curve, the pseudo-plateau at ~1.57 V is more developed for the 124th compared to the 65th cycle, while the other plateau shifts from ~1.99 V in the 65th to ~1.94 V in the 124th cycle and is slightly less pronounced. In total, a slight capacity gain is observed comparing the 65th to the 124th cycle. After the 124th cycle, the capacity steadily decreases, which is seen in the discharge/charge profiles as well. The same events observed in the discharge and charge curves of the 124th cycle occur in the 200th cycle, but are less pronounced and rather faint resulting in a lower specific capacity compared to the 124th cycle. The evolution of the potential plateaus are better visible in the *dQ/dV* curves (Figure S3) allowing determination of the exact potentials of the (pseudo-)plateaus.

It is noteworthy that the amount of consumed Na/f.u. for the initial discharging and charging (D/C) is very similar for $CuCrP_2S_6$ (D/C: 13.6/11.2 Na/f.u.) and for $Ni_2P_2S_6$ (D/C: 14.0/11.7 Na/f.u.),[36] which strengthens the assumption of a similar general reaction pathway for initial discharging and charging. For $Ni_2P_2S_6$ the discharge process delivered Ni, P and Na_2S as reaction products, while charging led to the formation of Ni_3S_2 besides probably some kind of phosphorus sulfide.[36] For $CuCrP_2S_6$, this would correspond to the formation of Cu, Cr, P and Na_2S in the discharged state, while charging may generate Cu and Cr sulfides or Cu–Cr sulfides and most probable phosphorus sulfides. However, the mechanistic processes of the initial cycle are described in more detail in section 3.3.

The initial dropping and recovery of specific capacity upon cycling is often observed for electrodes in SIBs and in many cases associated with alterations of the underlying conversion reaction mechanisms. However, different synergistic effects as for CuS are known as well causing an increasing capacity at the beginning of long-term measurements after a distinct capacity drop. However, the capacity recovery behavior observed for $CuCrP_2S_6$ differs from that of CuS.[57] Nevertheless, electrodes like $Ni_2P_2S_6$, CuV_2S_4 or $CuCrS_2$ indeed picture similar patterns during long-term cycling.[36,49,50] For these materials, the slow and steady recovery after an initial period of decreasing

capacity is caused by changes of the reaction mechanism, which is also very likely for $CuCrP_2S_6$ demonstrated by the shapes of the discharge and charge curves (Figure 3b, c) after an extended period of cycling. In this context, the two Cu containing materials CuV_2S_4 and $CuCrS_2$ are of special interest. It was reported that an extrusion mechanism leads to formation of elemental Cu in the early discharge stages, which first does not participate in the electrochemical reaction upon early long-term cycling, but in later stages presumably prevents detrimental formation and dissolution of polysulfides by formation of Cu sulfides.[49,50] However, we note that the quaternary $CuCrP_2S_6$ compound and its potential electrochemical reactions occurring during long-term cycling are probably more complex than those postulated for the ternary compounds. Therefore, phosphorus might as well play an important role regarding changes of the mechanisms during extended periods of cycling.

To determine the rate capability of the material, current rates of 0.2, 0.5, 1.0, 2.0, 3.0 and again 0.2 $A\,g^{-1}$ were applied for 10 cycles each (Figure 3d). The 10th cycle of the lowest current rate of 0.2 $A\,g^{-1}$ delivers a specific discharge capacity of 857 $mAh\,g^{-1}$. The successive increase of the applied current leads to lower specific discharge capacities in the 10th cycle of each current rate (Table 1).

Table 1. Observed specific capacities and corresponding capacity retentions at different current rates.

Current rate [$A\,g^{-1}$]	Specific capacity [$mAh\,g^{-1}$]	Capacity retention [%]
0.2	857	-
0.5	566	66
1.0	531	62
2.0	468	55
3.0	422	49
0.2	681	79

As observed in the long-term measurements, the capacity drops quickly for the first cycles. Because this initial period of declining capacity lasts for at least about 20 cycles in the long-term measurement, it can be assumed that this period strongly influences the first two current rates of the rate capability measurement. Accordingly, the value of the capacity retention going from 0.2 $A\,g^{-1}$ to 0.5 $A\,g^{-1}$ might be underdetermined. However, the specific capacities obtained from the highest rate of 3.0 $A\,g^{-1}$ (422 $mAh\,g^{-1}$) clearly show an excellent rate capability compared to the capacities obtained from the long-term experiments (current rate of 1.0 $A\,g^{-1}$: 409 $mAh\,g^{-1}$ after 200 cycles; peak performance after initial capacity drop: ~500 $mAh\,g^{-1}$). Starting from the 10th cycle with a current rate of 1.0 $A\,g^{-1}$ (531 $mAh\,g^{-1}$), the tolerance to higher currents is revealed. The corresponding capacity retentions amount to 88% and 79% for the current densities of 2.0 $A\,g^{-1}$ and 3.0 $A\,g^{-1}$ compared to a current rate of 1.0 $A\,g^{-1}$. The rate capability measurements clearly evidence that a considerable loss of capacity occurs switching from lower to higher current densities, whereas the capacity loss is quite small when switched between high current rates. After applying all current rates and using the initial current density, the capacity retention amounts to 79%, which in general indicates a good tolerance against high currents. Especially when taking into consideration that the observed specific capacity was still decreasing (as seen in long-term measurement) during the first 10 cycles, the capacity retention of 79% for the last 10 cycles might as well be underdetermined.

For comparison of obtained values, the long-term stability and rate capability of $CuCrP_2S_6$ is related to similar anode materials, such as other thiophosphates or pseudo-layered sulfides, and to different ternary as well as binary 3D materials and some composite electrodes as well (Table 2). We note that experiments for distinct materials are usually designed differ-

Table 2. Comparison between selected indicators of electrochemical performance of different anode materials and $CuCrP_2S_6$.

Anode material	Long-term stability capacity/current/cycles [$mAh\,g^{-1}$]/[$mA\,g^{-1}$]/[#]	Rate capability[a] capacity/current [$mAh\,g^{-1}$]/[$mA\,g^{-1}$]	Operating potential	Ref.
$CuCrP_2S_6$	409/1000/200	422/3000 468/2000	3.0–0.1	This work
$Ni_2P_2S_6$	621/1000/190	392/3000 488/2000	3.0–0.1	[36]
CuV_2S_4	580/700/250	232/2000	3.0–0.01	[49]
$CuCrS_2$	252/1500/500	158/2000	2.5–0.1	[50]
$CrPS_4$	687/1000/300	288/3000 346/2000	3.0–0.1	[56]
$NiCr_2S_4$	558/500/200	399/5000 492/2000	3.0–0.1	[58]
Fe_3S_4	486/500/300	140/9000 359/2000	3.0–0.5	[59]
$CuFeS_2$	444/500/700	180/5000 352/2000	3.0–0.3	[60]
$CuFe_2S_3$	422/500/1000	170/5000 301/2000	3.0–0.3	[61]
NiS_2	319/500/1000	253/5000 420/2000	2.9–0.4	[62]
NiS/rGO	483/200/100	393/2000	3.0–0.01	[63]
NiS/CNT	394/200/100	331/2000	3.0–0.01	[63]

[a] rate capability at maximum current and at 2 $A\,g^{-1}$ is shown.

ently and adjusted to the particular electrode (i.e. different current rates and operating potential ranges). Hence, an in-depth comparison would be inappropriate. Nevertheless, it is clearly visible that some materials are more tolerant against high currents, while others show better long-term stability. Besides, it shows that long-term performance and rate capability of $CuCrP_2S_6$ is within the same range of other electrode materials and therefore an appropriate overall electrochemical performance is obtained.

Investigation of the reaction mechanism via X-ray diffraction and CV analysis

X-ray powder diffraction

In order to gain insights into the electrochemical mechanism of the conversion reaction between $CuCrP_2S_6$ and Na in the first cycle, electrodes were discharged and charged to distinct states and subsequently characterized by PXRD. Electrodes of the phase pure sample were prepared on Al foil, while for samples with minor impurities, pressed powder electrodes were prepared. The discharge and charge profile of electrodes on Al foil (Figure 4a) shows minor deviations from the profiles of electrodes on Cu foil (see Figure 3b; inset) due to the different metal used as current collector (Cu vs. Al). In addition, a slightly larger capacity was obtained from the sample on Al, which is due to the lower current rate. The corresponding PXRD patterns (Figure 4b) reveal interesting details of the electrochemical reaction. At a low uptake of 0.5 Na/f.u., new reflections appeared at ~11.9 and ~5.9 °2θ and simultaneously the reflections at ~30.5, ~35.5 and ~53.5 °2θ gained intensity compared to the other reflections of $CuCrP_2S_6$. After uptake of 1 Na/f.u. reflections of $CuCrP_2S_6$ have lost a substantial amount of intensity, while the newly emerged reflections at ~11.9 and ~5.9 °2θ are the most intense reflections and additional reflections at ~23.9 and ~52.2 °2θ appeared. These reflections reached their maximum intensity after the uptake of 2 Na/f.u., whereas those at ~11.9, 23.9 and 52.3 °2θ slightly shift to ~11.8, 23.8 and 51.1 °2θ. No distinct reflections of the starting material $CuCrP_2S_6$ can be observed at this state of discharge, but a region of slightly enhanced intensity has developed at ~27.8–36.0 °2θ. Further discharging leads to diminishing intensities, while the reflection at 51.1 °2θ has shifted to ~50.8 °2θ after the uptake of 5 Na/f.u. After the uptake of 9 Na/f.u. only minor residues of the intermediate phase remain, while new reflections at ~23.3, 38.6, 43.3 and 55.8 °2θ can be observed for the completely discharged electrode. It is noteworthy that the reflection at ~43.3 °2θ can be observed as early as ~2 Na/f.u. After recharging the electrode, the only observable reflections are located at ~38.7 and 55.9 °2θ.

Taking a closer look at the important states of discharge (Figure 5a–d) gives a more detailed insight into the ongoing mechanism. PXRD patterns of the $CuCrP_2S_6$ electrode collected after the complete discharge (Figure 5a) evidence the formation of nanoscopic elemental Cu and Na_2S. The high background of the pattern is an indication of amorphous phases present in the discharged sample, which is not surprising as no signs of crystalline phases containing Cr or P are observable. X-ray amorphous elemental Cr in discharged electrodes was previously reported for the anode material $CuCrS_2$.[50] Taking the formation of Na_2S and metallic Cu into account and assuming that Cr is reduced to its metallic state, an electrochemical reaction according to Equation (1) involving 12 Na/f.u. is postulated. However, the actual observed Na uptake of ~15 Na/f.u. is larger than required for the proposed reaction. In this context, the uptake of an excess of Na often is explained by Na_3P formation for MTP electrodes. Indeed, no evidence for the

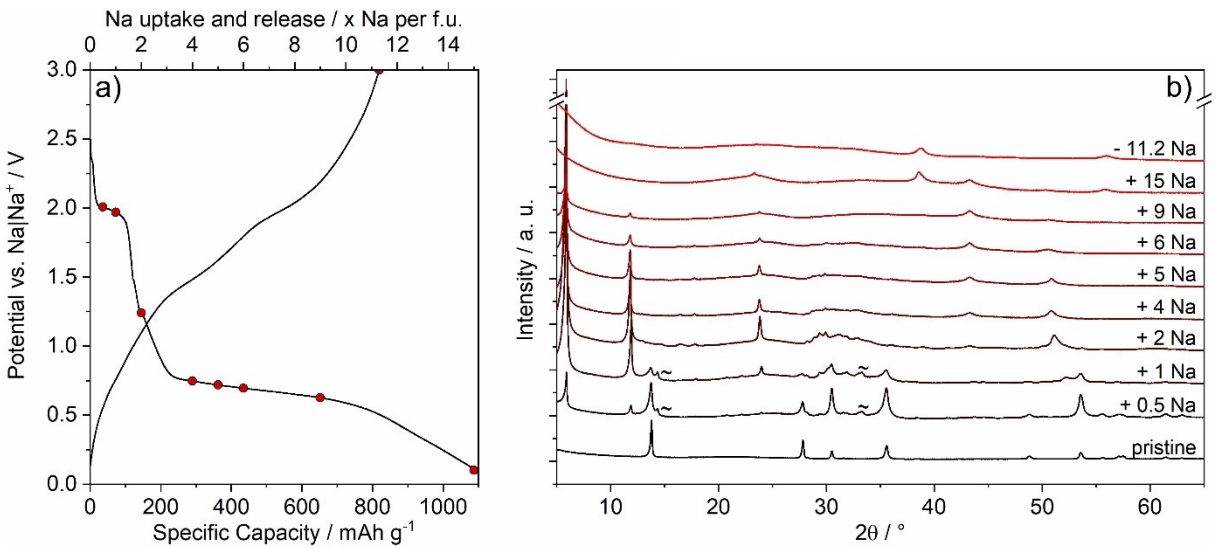

Figure 4. a) Discharge and charge profile of a $CuCrP_2S_6$ film electrode casted on Al foil. The uptake/release of Na of the investigated samples is indicated by red dots. b) PXRD patterns of $CuCrP_2S_6$ electrodes collected at different states of charge. The pattern marked with "+15 Na" indicates the completely discharged sample, while the pattern denoted with "-11.2 Na" was obtained from the recharged electrode. Reflections marked with ~ originate from minor impurities of $CrPS_4$.

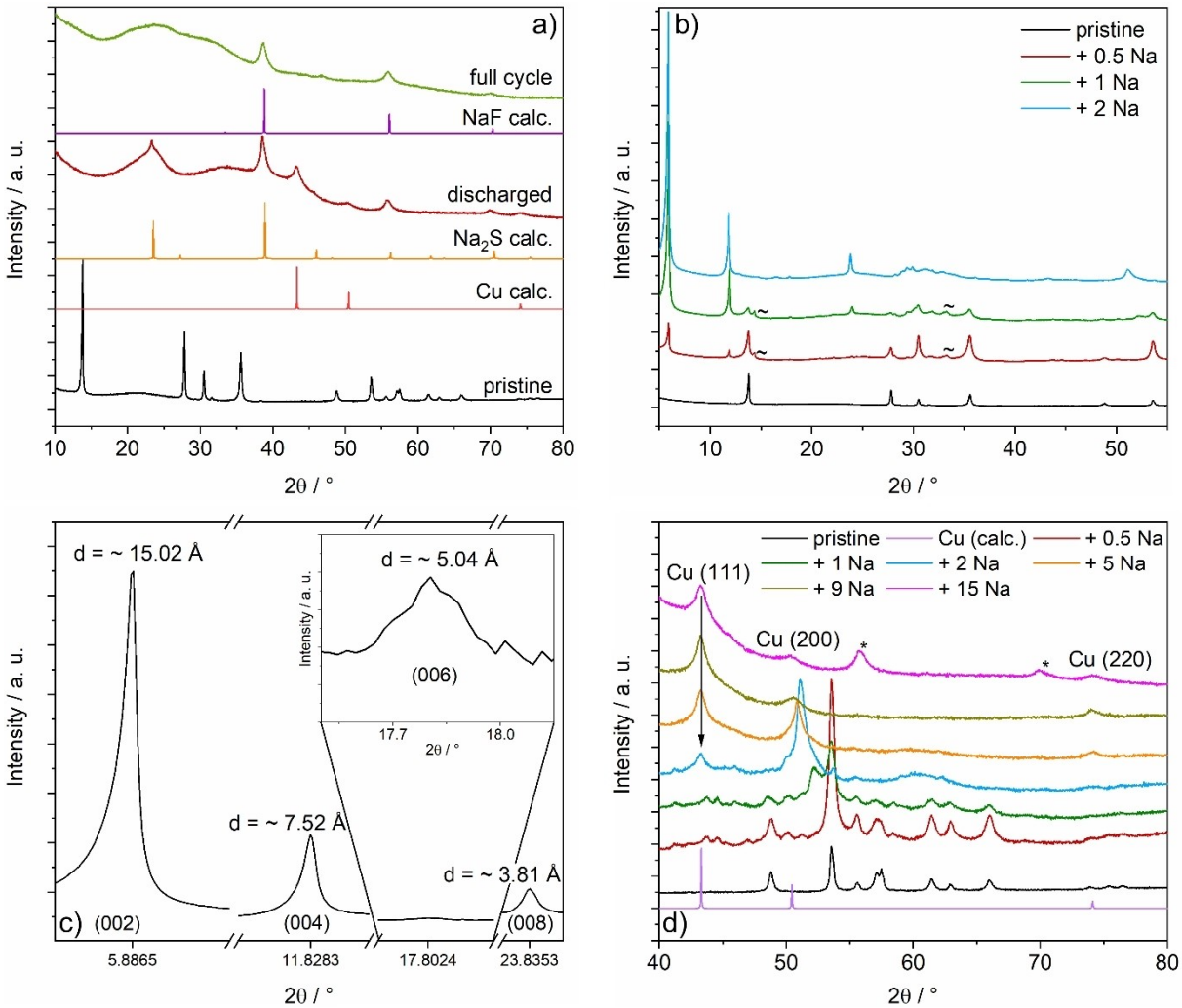

Figure 5. a) PXRD patterns of pristine $CuCrP_2S_6$, the completely discharged and the recharged electrode compared with simulated patterns of NaF,[73] Na_2S[74] and fcc Cu.[75] b) PXRD patterns of the early states of discharge up to 2 Na/f.u. The reflections marked with ~ correspond to minor impurities of $CrPS_4$. (c) Selected areas of the PXRD pattern after an uptake of 2 Na/f.u. to highlight the series of (00 *l*) reflections. d) PXRD patterns of different discharge states compared with a simulated pattern of fcc Cu[75] evidencing the extrusion of Cu in the early discharge process. Reflections marked with * arise from the formation of Na_2S at the completely discharged state.

formation of Na_3P has been presented yet, and often the experimentally determined specific capacities do not match the required Na uptake for the proposed mechanisms involving Na_3P formation.[35,64–66] In contrast, some investigations of MTPs explicitly noticed that no signs of Na_3P were found after discharging.[36,55,56] Therefore, as long as no reliable evidence of Na_3P is presented, its formation during discharging should be considered at least very carefully. Furthermore, SEI formation and other side reactions can lead to even higher initial discharge capacities. In consequence, when actual Na_3P formation takes place, an enhanced Na uptake is expected. Hence, in the case of $CuCrP_2S_6$, the difference of ~3 Na/f.u. is most likely due to a combination of SEI formation and co-intercalation of solvent molecule from the electrolyte. Additionally, the excess of consumed Na in the initial cycle is within the same magnitude as for the previously studied active material $Ni_2P_2S_6$ with an extra consumption of ~2 Na/f.u., where no signs of Na_3P were observed either.[36] Regarding the PXRD pattern collected after recharging the $CuCrP_2S_6$ electrode, only Bragg reflections of NaF are observable, which is a commonly observed SEI compound in SIBs.[67–71] The fact that NaF can be observed in the PXRD pattern indicates that a larger amount of SEI must have formed during discharging. Because no crystalline phase other than NaF is observed in the PXRD pattern of the recharged sample, an amorphization of the electrode material after the first cycle is most probable. The specific capacity for the recharged sample is ~820 mAh g^{-1} corresponding to ~11.3 Na/f.u.

PXRD patterns of the early discharge states (Figure 5b) clearly show that reflections of the starting material disappeared up to 2 Na/f.u., while new reflections of an intermediate phase successively develop with increasing Na content. Apart from a region with slightly enhanced background intensity (~ 27.8–36.0 °2θ), the pattern (2 Na/f.u.) is characterized by one weak and three pronounced and relatively sharp reflections located at ~5.9, 11.8, 17.8 (very weak) and 23.8 °2θ. Detailed

examinations (Figure 5c) of the reflection positions reveal that these belong to the (00 *l*) series. Assuming that the space group does not change upon Na uptake maintaining the general reflection condition for the (00 *l*) series of $l = 2n$, the *c* parameter increases from ~13.42 Å to ~31.43 Å, while the resulting unit cell likely contains twice as many layers (N = 4) as the unit cell of the pristine $CuCrP_2S_6$ (N = 2). The corresponding interlayer expansion amounts to ~1.1 Å, which is in accordance with the ionic radius of Na^+ in four- to sixfold coordination geometry (0.99 Å - 1.02 Å)[72] and indicates the intercalation of ~1 Na/f.u. into the van der Waals gaps of $CuCrP_2S_6$ after the uptake of 2 Na/f.u. The difference of ~1 Na/f.u. most likely occupies the octahedral sites within the layers, where Cu^+ cations have been reduced and replaced by Na^+. As mentioned earlier, another reflection at ~51.1 °2θ and the region of enhanced intensity between ~27.8 and 36.0 °2θ most likely belong to this intermediate phase. However, based on the few sharp and the region of blurry reflections, it is impossible to propose a reliable structure model for the intermediate phase. Especially, the smeared intensities at ~27.8 to 36.0 °2θ are indications for additional structural disorder making a structure prediction even more difficult. Nevertheless, the occurrence of reflections of the (00 *l*) series (Figure 5b, c) clearly demonstrates that the layered structure is maintained, and the interlayer expansion suggests intercalation of Na^+. Furthermore, the observed formation of elemental Cu after the uptake of 2 Na/f.u. (Figure 5d) strongly indicates the extrusion of Cu by Na.

Based on the findings in the early discharge states and the presence of Na_2S and elemental Cu at the completely discharged state, we propose the following simplified reaction pathway for the first discharge process, $x < 1$ [Eq. (2)]:

$$CuCrP_2S_6 \xrightarrow{+2\ Na} Na_2Cu_{1-x}CrP_2S_6 + xCu \xrightarrow{+10\ Na} Cu + Cr + \frac{2}{n}P_n + 6Na_2S \quad (2)$$

We note that some portion of Cu potentially remains in the intermediate phase as observed for *e.g.* $CuCrS_2$ electrodes.[50] Hence, at 2 Na/f.u., residual Cu^+ and intercalated Na^+ coexist in $Na_2Cu_{1-x}CrP_2S_6$ and the corresponding reaction is a combination of reduction/extrusion and intercalation. For the reaction pathway towards the end of the process, a conversion is most likely as supported by the detection of Na_2S. We particularly underline that no hints for formation of any Na_xP phases were found. Even if Na_xP was formed in the fully discharged state, one would expect that the capacity delivered upon recharging is larger than observed (~11.3 Na/f.u.) and similar to the discharge capacity (~15 Na/f.u.). Therefore, the formation of P(0) is assumed in the form of amorphous, polymeric phosphorus. The investigations of the recharged sample only prove the presence of NaF, preventing the postulation of a detailed reaction pathway for the charging process. Nevertheless, assuming a similar pathway as observed for $Ni_2P_2S_6$,[36] the formation of Cu, Cr and P sulfides seems reasonable.

Cyclic voltammetry

In order to assess and discuss the results from an electrochemical perspective, CV curves of the $CuCrP_2S_6$ electrode (Figure 6) were recorded. The curve of the initial cycle exhibits two pronounced and one weak reduction peaks, a shoulder and three broad oxidation events. The first reduction occurs at ~1.94 V (peak 1) and is assigned to the intercalation of Na^+ into the structure and the extrusion and resulting reduction of Cu^+

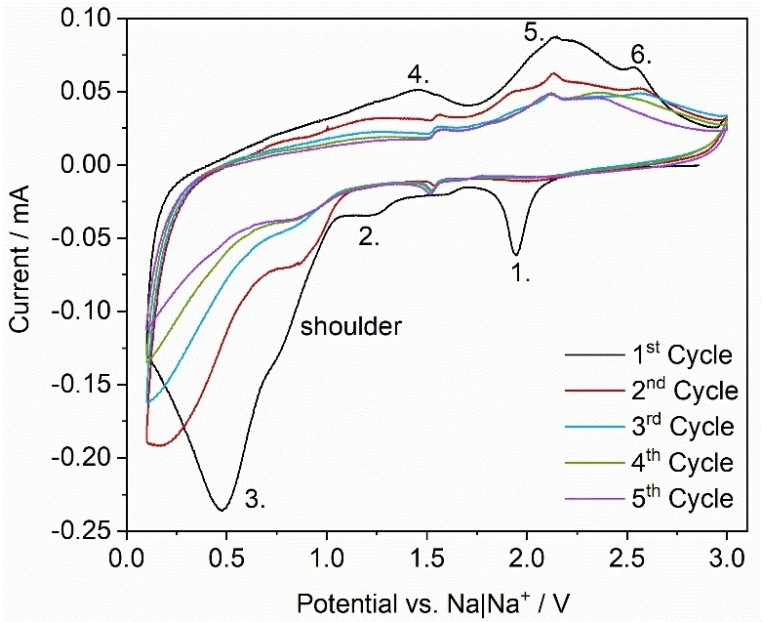

Figure 6. CV curves of the first 5 cycles recorded with a scan rate of 0.1 mV s^{-1} within a potential range of 3.0 to 0.1 V.

to metallic Cu. The most intense reduction peak at ~0.48 V (peak 3) is assigned to the reduction of Cr^{3+} to Cr^0 in accordance with electrochemical data from Cr_3S_4 and $NiCr_2S_4$.[58] However, this peak is very broad and potentially superposes smaller signals. Furthermore, a shoulder at ~0.77 V and a weak signal at ~1.21 V (peak 2) occur, which likely are associated with a (two-step) reduction of P^{4+}. Additionally, SEI formation likely contributes to the broadening of reduction peak 3 and/or the formation of the shoulder.

The first oxidation peak is observed at ~1.45 V (peak 4), which is assigned to the oxidation of Cr^0. The oxidation events occurring at ~2.13 V (peak 5) and ~2.54 V (peak 6) arise from the oxidation of P and Cu, respectively. The blurred appearance of peak 5 thereby is an indication of the occurrence of several oxidation processes, which potentially is due to a multi-step oxidation of P, similar to the observation made for the reduction process. We note that the assignment of the redox events was based on the information gathered by PXRD combined with the standard potentials of the redox couples Cu^+/Cu, $H_4P_2O_6/H_3PO_3$, $H_3PO_3/P(red)$ and Cr^{3+}/Cr amounting to $E^0 = +0.52$ V; $E^0 = +0.38$ V; $E^0 = -0.45$ V; $E^0 = -0.74$ V, respectively.[76]

CV curves of cycles 2–5 differ from the first cycle, but are similar in appearance to each other, which is a typical sign of a conversion-type reaction. The most obvious differences are absence of peak 1 and shifting of peak 2 to lower potentials. Furthermore, the shape of the oxidation peaks strongly changed and their intensity decreased. The shift of the reduction peak 2 accompanied by decreasing intensity likely arises from a changing discharge process during the first cycles. However, SEI formation lasting for several cycles might also influence peak 2. The shoulder (~0.77 V in the 1st cycle), which is still visible in the 2nd cycle, lost intensity and might be a sign of ongoing SEI formation after the 1st cycle as well.

To summarize, the findings from the CV experiment support the results obtained from PXRD measurements and shed light on the underlying electrochemical processes. The proposed discharging reaction pathway [Eq. (2)], which is based on PXRD investigations, match the redox processes visualized by the CV curves and therefore seems plausible. The CV experiment further confirms conversion-like behavior of the electrode, which already was assumed as a result of the electrochemical characterization. However, it is noteworthy that CV measurements usually do not provide sufficient information to unveil details of conversion reactions individually. Therefore, the suggestions made here, which solely were based on CV measurements should be treated as such and must not be over-interpreted.

Conclusion

The layered compound $CuCrP_2S_6$ was successfully obtained from chemical vapor transport reaction and phase purity could be improved significantly by varying the synthesis parameters. Galvanostatic measurements yielded the very large specific capacity of 1011 mAh g^{-1} in the first cycle, which dropped to 461 mAh g^{-1} within 65 cycles, followed by a recovery (124th cycle: 504 mAh g^{-1}) and decreased to 409 mAh g^{-1} after 200 cycles. Rate capability measurements delivered 422 mAh g^{-1} at a current density of 3.0 A g^{-1} and revealed a decent tolerance against high current densities. The observed fluctuations of capacities in the long-term measurement are most likely due to changes of the underlying reaction mechanism, which is a common observation for conversion reactions. At the beginning of Na uptake an intercalation reaction occurs accompanied by an expansion of the interlayer space of the structure. The Na insertion leads to a reduction of Cu^+, which is expelled as nanocrystalline metallic Cu from the host, i.e. the mechanism may be described as intercalation-reduction-extrusion reaction. Increasing the Na content results in a successive decomposition of the intermediate phase and only elemental Cu and nanocrystalline Na_2S can be observed in the PXRD pattern of the completely discharged electrode. For the recharged sample, the presence of NaF is evidenced by PXRD, which can be attributed to the formation of a SEI layer.

The large value of the specific charge capacity can be explained by oxidation of Cu, P and Cr, despite no reflections of Cu, P and/or Cr sulfides are observed in the PXRD pattern of the recharged electrode. This observation suggests that the phases containing Cu, P and Cr are in the nanocrystalline/amorphous state. Considering the results and the values of the experimentally obtained specific capacity, a discharge reaction involving 12 Na/f.u. [Eq. (2)] is most likely, while charging releases 11.3 Na/f.u. and several reactions may be postulated depending on the assumptions made as shown in the formal Equations (3–7):

$$Cu + Cr + \frac{2}{n}P_n + 6Na_2S \rightarrow \frac{1}{6}Cu_2S + CrS + \frac{1}{2}P_4S_9 + 11\frac{1}{3}Na + \frac{1}{3}Na_2S + \frac{2}{3}Cu \quad (3)$$

$$Cu + Cr + \frac{2}{n}P_n + 6Na_2S \rightarrow \frac{1}{3}Cu_2S + \frac{1}{3}Cr_3S_4 + \frac{1}{2}P_4S_8 + 11\frac{1}{3}Na + \frac{1}{3}Na_2S + \frac{1}{3}Cu \quad (4)$$

$$Cu + Cr + \frac{2}{n}P_n + 6Na_2S \rightarrow \frac{1}{6}Cu_2S + \frac{1}{2}Cr_2S_3 + \frac{1}{2}P_4S_8 + 11\frac{1}{3}Na + \frac{1}{3}Na_2S + \frac{2}{3}Cu \quad (5)$$

$$Cu + Cr + \frac{2}{n}P_n + 6Na_2S \rightarrow Cu + \frac{2}{3}CrS + \frac{1}{2}P_4S_{10} + 11\frac{1}{3}Na + \frac{1}{3}Na_2S + \frac{1}{3}Cr \quad (6)$$

$$Cu + Cr + \frac{2}{n}P_n + 6Na_2S \rightarrow Cu + \frac{7}{18}Cr_2S_3 + \frac{1}{2}P_4S_9 + 11\frac{1}{3}Na + \frac{1}{3}Na_2S + \frac{2}{9}Cr \quad (7)$$

We note that these are formal reactions, which demonstrate the plethora of possible oxidation products and highlight the enormous difficulties formulating a distinct mechanism in the case where only amorphous/nanocrystalline products are formed. Especially for the P-sulfides, the chemical formula should not imply that these well-known compounds actually are generated, but they rather account for the experimental capacity. The CV curves indicate that at least partial oxidation of Cu, Cr, and P occurs making Equations (6) and (7) less likely.

Experimental Section

Synthesis

$CuCrP_2S_6$ was synthesized by chemical vapor transport reaction. Stoichiometric amounts of copper (Chempur, 99.95%) and chromium (Alfa Aesar, 99.94%) were mixed with an excess (6 wt%) of red phosphorus (Knapsack AG, 99.9999%) and sulfur (Chempur, 99.999%) and sealed in a quartz glass ampoule ($<10^{-4}$ mbar). The quartz tube was then placed in a tube furnace and heated to 723 K within 4 h and maintained at this temperature for 24 h. Afterwards, the temperature was increased within 2.5 h to 973 K. When this temperature was reached, a temperature gradient to 953 K was established to start the chemical vapor transport. The reaction was carried out for 14 d. It is noteworthy that this quaternary system is extremely sensitive to the slightest alterations and thus many approaches were necessary to obtain the phase pure product. However, it was always possible to manually separate $CuCrP_2S_6$ from the $CrPS_4$ side product, when the reaction parameters were adjusted optimally. By variation of reaction parameters, the ratio of $CrPS_4$ to $CuCrP_2S_6$ could be altered in favor of $CuCrP_2S_6$, but ultimately the formation of $CrPS_4$ could not be fully avoided. The product was obtained as shiny black plate-like crystals.

Electrochemical tests

For electrode preparation, 70 wt% of $CuCrP_2S_6$ was mixed together with 20 wt% of SUPER C65 (Timcal, Switzerland) and 10 wt% of polyvinylidene difluoride (PVDF, Solvay, Germany) and afterwards suspended in *N*-methyl-2-pyrrolidone (NMP, Fisher Bioreagens, 99.8%). The obtained suspension was cast onto Cu foil using the doctor-blade method. The electrode was dried over night at room temperature and additionally several hours in a vacuum oven at 333 K. For battery assembly, circular electrodes with diameters of 10 mm were punched out and transferred into Swagelok® type cells together with a Celgard® membrane and glass fibre filter (Whatman™, United Kingdom) both serving as separators. For final assembly, the cells were transferred into an argon glovebox (99.999% Ar, MBraun Unilab, <1 ppm H_2O; <1 ppm O_2) and sodium metal acting as counter electrode and a 1 M solution of $NaCF_3SO_3$ (abcr, 98%) in bis(2-methoxyethyl)ether (Diglyme, Acros Organics, 99+%, extra dry) serving as electrolyte were added. Galvanostatic long-term measurements were conducted using a Neware 8 channel battery analyzer, applying current rates of 1 $A\,g^{-1}$ within a voltage range of 3.0 to 0.1 V. Constant current-constant voltage (CCCV) charge mode was applied with a cutoff current density of 0.2 $A\,g^{-1}$. For rate capability measurements, current densities between 0.2 and 3.0 $A\,g^{-1}$ were applied within the same voltage range. Cyclic voltammetry (CV) measurements were conducted using a Zahner XPOT with a scanning rate of 0.1 $mV\,s^{-1}$ between 3.0 and 0.1 V. In order to gather information about the electrochemical reaction, galvanostatic measurements were interrupted after a defined uptake/release of Na. For these experiments, pressed powder electrodes and film electrodes casted on Al foil were used. The electrodes on Al foil were prepared as described above. For powder electrodes, a mixture of 70 wt% $CuCrP_2S_6$ and 30 wt% SUPER C65 was pressed into pellets and used in Swagelok® cells as described for the film cells. A low current rate of C/20 was applied for these experiments. After the uptake/release of a predetermined amount of Na, the electrodes were recovered, rinsed with Diglyme and dried for 24 h in an argon-filled glovebox. The samples were transferred into borosilicate capillaries and sealed in argon atmosphere for further measurements.

Material characterizations

Powder X-ray diffraction (PXRD) measurements were performed using Cu K_α radiation (1.54058 Å) with a PANalytical diffractometer equipped with a 1D PIXcel detector in Debye-Scherrer geometry. Elemental CHNS analysis was done with a vario MICRO cube elemental analyzer (Elementar) using sulphanilamide as standard material. EDX and SEM experiments were conducted using a Philips ESEM XL 30 system equipped with an EDAX New XL-30 detector.

Supporting Information

Details about different synthesis approaches; additional PXRD patterns; results of EDX and elemental analysis, *dQ/dV* curves

Acknowledgements

Financial support by the State of Schleswig-Holstein is gratefully acknowledged. Open Access funding enabled and organized by Projekt DEAL.

Conflict of Interest

The authors declare no conflict of interest.

Data Availability Statement

The data that support the findings of this study are available from the corresponding author upon reasonable request.

Keywords: $CuCrP_2S_6$ · anode material · sodium-ion battery · reaction mechanisms · X-ray diffraction · intercalation · extrusion

[1] J.-Y. Hwang, S.-T. Myung, Y.-K. Sun, *Chem. Soc. Rev.* **2017**, *46*, 3529–3614.
[2] E. de la Llave, V. Borgel, K.-J. Park, J.-Y. Hwang, Y.-K. Sun, P. Hartmann, F.-F. Chesneau, D. Aurbach, *ACS Appl. Mater. Interfaces* **2016**, *8*, 1867–1875.
[3] D. Larcher, J.-M. Tarascon, *Nat. Chem.* **2015**, *7*, 19–29.
[4] N. Yabuuchi, K. Kubota, M. Dahbi, S. Komaba, *Chem. Rev.* **2014**, *114*, 11636–11682.
[5] M. D. Slater, D. Kim, E. Lee, C. S. Johnson, *Adv. Funct. Mater.* **2013**, *23*, 947–958.

[6] J. Deng, W.-B. Luo, S.-L. Chou, H.-K. Liu, S.-X. Dou, *Adv. Energy Mater.* **2018**, *8*, 1701428.
[7] Y. Kim, K.-H. Ha, S. M. Oh, K. T. Lee, *Chem. Eur. J.* **2014**, *20*, 11980–11992.
[8] K. M. Abraham, *ACS Energy Lett.* **2020**, *5*, 3544–3547.
[9] D. A. Stevens, J. R. Dahn, *J. Electrochem. Soc.* **2001**, *148*, A803–A811.
[10] K. Nobuhara, H. Nakayama, M. Nose, S. Nakanishi, H. Iba, *J. Power Sources* **2013**, *243*, 585–587.
[11] J. Sangster, *J. Phase Equilib. Diffus.* **2007**, *28*, 571–579.
[12] Y. Okamoto, *J. Phys. Chem. C* **2014**, *118*, 16–19.
[13] D.-Y. Kim, D.-H. Kim, S.-H. Kim, E.-K. Lee, S.-K. Park, J.-W. Lee, Y.-S. Yun, S.-Y. Choi, J. Kang, *Nanomaterials* **2019**, *9*, 793.
[14] B. Xiao, T. Rojo, X. Li, *ChemSusChem* **2019**, *12*, 133–144.
[15] I. El Moctar, Q. Ni, Y. Bai, F. Wu, C. Wu, *Funct. Mater. Lett.* **2018**, *11*, 1830003.
[16] E. Irisarri, A. Ponrouch, M. R. Palacin, *J. Electrochem. Soc.* **2015**, *162*, A2476–A2482.
[17] P. K. Nayak, L. Yang, W. Brehm, P. Adelhelm, *Angew. Chem. Int. Ed.* **2018**, *57*, 102–120; *Angew. Chem.* **2018**, *130*, 106–126.
[18] Y. Xiao, S. H. Lee, Y.-K. Sun, *Adv. Energy Mater.* **2017**, *7*, 1601329.
[19] W. Kang, Y. Wang, J. Xu, *J. Mater. Chem. A* **2017**, *5*, 7667–7690.
[20] J. Mao, T. Zhou, Y. Zheng, H. Gao, H. kun Liu, Z. Guo, *J. Mater. Chem. A* **2018**, *6*, 3284–3303.
[21] Z. Hu, Q. Liu, S.-L. Chou, S.-X. Dou, *Adv. Mater.* **2017**, *29*, 1700606.
[22] X. Y. Yu, X. W. (David) Lou, *Adv. Energy Mater.* **2018**, *8*, 1701592.
[23] Y. Liu, C. Yang, Q. Zhang, M. Liu, *Energy Storage Mater.* **2019**, *22*, 66–95.
[24] M. Lao, Y. Zhang, W. Luo, Q. Yan, W. Sun, S. X. Dou, *Adv. Mater.* **2017**, *29*, 1700622.
[25] L. Li, Y. Zheng, S. Zhang, J. Yang, Z. Shao, Z. Guo, *Energy Environ. Sci.* **2018**, *11*, 2310–2340.
[26] Q. Xia, W. Li, Z. Miao, S. Chou, H. Liu, *Nano Res.* **2017**, *10*, 4055–4081.
[27] H. Liu, K. Hu, D. Yan, R. Chen, Y. Zou, H. Liu, S. Wang, *Adv. Mater.* **2018**, *30*, 1800295.
[28] T. Wang, D. Su, D. Shanmukaraj, T. Rojo, M. Armand, G. Wang, *Electrochem. Energy Rev.* **2018**, *1*, 200–237.
[29] F. Klein, B. Jache, A. Bhide, P. Adelhelm, *Phys. Chem. Chem. Phys.* **2013**, *15*, 15876–15887.
[30] M. C. Friedel, *C. R. Hebd. Seances Acad. Sci.* **1894**, *119*, 260–264.
[31] M. A. Susner, M. Chyasnavichyus, M. A. McGuire, P. Ganesh, P. Maksymovych, *Adv. Mater.* **2017**, *29*, 1602852.
[32] R. Dangol, Z. Dai, A. Chaturvedi, Y. Zheng, Y. Zhang, K. Ngoc Dinh, B. Li, Y. Zong, Q. Yan, *Nanoscale* **2018**, *10*, 4890–4896.
[33] F. Wang, T. A. Shifa, P. Yu, P. He, Y. Liu, F. Wang, Z. Wang, X. Zhan, X. Lou, F. Xia, J. He, *Adv. Funct. Mater.* **2018**, *28*, 1802151.
[34] K. Du, X. Wang, Y. Liu, P. Hu, M. I. B. Utama, C. K. Gan, Q. Xiong, C. Kloc, *ACS Nano* **2016**, *10*, 1738–1743.
[35] Q. Liang, Y. Zheng, C. Du, Y. Luo, J. Zhang, B. Li, Y. Zong, Q. Yan, *Small Methods* **2017**, *1*, 1700304.
[36] J. van Dinter, K. Synnatschke, T. A. Engesser, S. Indris, N. Wolff, O. Gronenberg, M. Etter, G. Cibin, L. Kienle, C. Backes, W. Bensch, *J. Mater. Chem. A* **2020**, *8*, 22401–22415.
[37] G. Ouvrard, R. Fréour, R. Brec, J. Rouxel, *Mater. Res. Bull.* **1985**, *20*, 1053–1062.
[38] W. Klingen, R. Ott, H. Hahn, *Z. Anorg. Allg. Chem.* **1973**, *396*, 271–278.
[39] E. Prouzet, G. Ouvrard, R. Brec, *Mater. Res. Bull.* **1986**, *21*, 195–200.
[40] G. Ouvrard, R. Brec, J. Rouxel, *Mater. Res. Bull.* **1985**, *20*, 1181–1189.
[41] R. Brec, *Solid State Ionics* **1986**, *22*, 3–30.
[42] M. Evain, R. Brec, M.-H. Whangbo, *J. Solid State Chem.* **1987**, *71*, 244–262.
[43] P. Colombet, A. Leblanc, M. Danot, J. Rouxel, *J. Solid State Chem.* **1982**, *41*, 174–184.
[44] V. Maisonneuve, V. B. Cajipe, C. Payen, *Chem. Mater.* **1993**, *5*, 758–760.
[45] K. Momma, F. Izumi, *J. Appl. Crystallogr.* **2011**, *44*, 1272–1276.
[46] V. Bodenez, L. Dupont, M. Morcrette, C. Surcin, D. W. Murphy, J.-M. Tarascon, *Chem. Mater.* **2006**, *18*, 4278–4287.
[47] V. Bodenez, L. Dupont, L. Laffont, A. R. Armstrong, K. M. Shaju, P. G. Bruce, J.-M. Tarascon, *J. Mater. Chem.* **2007**, *17*, 3238–3247.
[48] W. Bensch, J. Ophey, H. Hain, H. Gesswein, D. Chen, R. Mönig, P. A. Gruber, S. Indris, *Phys. Chem. Chem. Phys.* **2012**, *14*, 7509–7516.
[49] M. Krengel, A.-L. Hansen, M. Kaus, S. Indris, N. Wolff, L. Kienle, D. Westfal, W. Bensch, *ACS Appl. Mater. Interfaces* **2017**, *9*, 21283–21291.
[50] M. Krengel, A.-L. Hansen, F. Hartmann, J. van Dinter, W. Bensch, *Batteries & Supercaps* **2018**, *1*, 176–183.
[51] A. R. Wildes, V. Simonet, E. Ressouche, R. Ballou, G. J. McIntyre, *J. Phys. Condens. Matter* **2017**, *29*, 455801.
[52] A. R. Wildes, V. Simonet, E. Ressouche, G. J. McIntyre, M. Avdeev, E. Suard, S. A. J. Kimber, D. Lançon, G. Pepe, B. Moubaraki, T. J. Hicks, *Phys. Rev. B* **2015**, *92*, 224408.
[53] C. Murayama, M. Okabe, D. Urushihara, T. Asaka, K. Fukuda, M. Isobe, K. Yamamoto, Y. Matsushita, *J. Appl. Phys.* **2016**, *120*, 142114.
[54] P. Fragnaud, E. Prouzet, R. Brec, *J. Mater. Res.* **1992**, *7*, 1839–1846.
[55] W. Brehm, A. L. Santhosha, Z. Zhang, C. Neumann, A. Turchanin, A. Martin, N. Pinna, M. Seyring, M. Rettenmayr, J. R. Buchheim, P. Adelhelm, *Adv. Funct. Mater.* **2020**, *30*, 1910583.
[56] J. van Dinter, S. Indris, A. Bitter, D. Grantz, G. Cibin, M. Etter, W. Bensch, *ACS Appl. Mater. Interfaces* **2021**, *13*, 54936–54950.
[57] J. Y. Park, S. J. Kim, K. Yim, K. S. Dae, Y. Lee, K. P. Dao, J. S. Park, H. B. Jeong, J. H. Chang, H. K. Seo, C. W. Ahn, J. M. Yuk, *Adv. Sci.* **2019**, *6*, 1900264.
[58] F. Hartmann, M. Etter, G. Cibin, L. Liers, H. Terraschke, W. Bensch, *Adv. Mater.* **2021**, *33*, 2101576.
[59] F. Hartmann, M. Etter, G. Cibin, H. Groß, L. Kienle, W. Bensch, *Nanoscale* **2022**, *14*, 2696-2710. .
[60] S. Senkale, S. Indris, M. Etter, W. Bensch, *ACS Appl. Mater. Interfaces* **2021**, *13*, 26034–26045.
[61] S. Senkale, G. Cibin, A. V. Chadwick, W. Bensch, *ACS Appl. Mater. Interfaces* **2021**, *13*, 58552–58565.
[62] R. Sun, S. Liu, Q. Wei, J. Sheng, S. Zhu, Q. An, L. Mai, *Small* **2017**, *13*, 1701744.
[63] J. Wang, D. Cao, G. Yang, Y. Yang, H. Wang, *J. Solid State Electrochem.* **2017**, *21*, 3047–3055.
[64] Q. Liang, Y. Zheng, C. Du, Y. Luo, J. Zhao, H. Ren, J. Xu, Q. Yan, *ACS Nano* **2018**, *12*, 12902–12911.
[65] Y. Sang, L. Wang, X. Cao, G. Ding, Y. Ding, Y. Hao, N. Xu, H. Yu, L. Li, S. Peng, *J. Alloys Compd.* **2020**, *831*, 154775.
[66] L. Li, H. Jiang, N. Xu, X. Lian, H. Huang, H. Geng, S. Peng, *J. Mater. Chem. A* **2021**, *9*, 17336–17343.
[67] J. Zhang, D.-W. Wang, W. Lv, S. Zhang, Q. Liang, D. Zheng, F. Kang, Q.-H. Yang, *Energy Environ. Sci.* **2017**, *10*, 370–376.
[68] J. Fondard, E. Irisarri, C. Courrèges, M. R. Palacin, A. Ponrouch, R. Dedryvère, *J. Electrochem. Soc.* **2020**, *167*, 070526.
[69] F. Wu, N. Zhu, Y. Bai, Y. Li, Z. Wang, Q. Ni, H. Wang, C. Wu, *Nano Energy* **2018**, *51*, 524–532.
[70] L. A. Ma, A. J. Naylor, L. Nyholm, R. Younesi, *Angew. Chem. Int. Ed.* **2021**, *60*, 4855–4863; *Angew. Chem.* **2021**, *133*, 4905–4913.
[71] J. Song, B. Xiao, Y. Lin, K. Xu, X. Li, *Adv. Energy Mater.* **2018**, *8*, 1703082.
[72] R. D. Shannon, *Acta Crystallogr. Sect. A* **1976**, *32*, 751–767.
[73] Y. Shirako, Y. G. Shi, A. Aimi, D. Mori, H. Kojitani, K. Yamaura, Y. Inaguma, M. Akaogi, *J. Solid State Chem.* **2012**, *191*, 167–174.
[74] E. Zintl, A. Harder, B. Dauth, *Z. Elektrochem. Angew. Phys. Chem.* **1934**, *40*, 588–593.
[75] H. M. Otte, *J. Appl. Phys.* **1961**, *32*, 1536–1546.
[76] A. J. Bard, R. Parsons, J. Jordan, *Standard Potentials in Aqueous Solution*, Marcel Dekker, New York, **1985**.

Manuscript received: January 5, 2022
Revised manuscript received: February 24, 2022
Accepted manuscript online: February 28, 2022